

Laser-Assisted Synthesis of Ag₂S-Quantum-Dot-in-Perovskite Matrix and Its Application in Broadband Photodetectors

Chen Zhao, Cailing Chen, Ran Wei, Yuting Zou, Wenchi Kong, Tao Huang, Zhi Yu, Jianjun Yang, Feng Li, Yu Han,* Chunlei Guo,* and Weili Yu*

Halide perovskites are widely explored as efficient photoresponsive materials for optoelectronic devices. However, understanding and controlling their underlying optical and electrical properties remains limited. Here, a novel approach is developed by introducing silver sulfide (Ag₂S) quantum dots (QDs) into an MAPbBr₃ single crystal. The high-quality Ag₂S-quantum-dot-in-perovskite (Ag₂S-QDiP) matrixes synthesized through a laser-assisted inverse temperature crystallization (LA-ITC) strategy show broadband light-sensitive wavelength from 550 to over 1000 nm, and a balanced carriers mobility facilitates their transmission and collection. A Ag₂S-QDiP-enabled photodetector is demonstrated, which exhibits considerably enhanced responsivity and detectivity of 1.17 A W⁻¹ and 6.24 × 10¹⁴ Jones at 532 nm, and 57.69 mA W⁻¹ and 1.03 × 10¹¹ Jones at 1064 nm, respectively. The enhanced performance in the near-infrared (NIR) region can be attributed to the discrete heterojunction formed between MAPbBr₃ and Ag₂S QDs, which enhances the light absorption in the NIR range and facilitates photogenerated excitons' separation at the interface. The facile synthesis process, the more balanced transport behavior, and the ensuing improved device performance highlight introducing QDs into perovskite single crystal as an efficient strategy for tuning fundamental properties of perovskite and for developing high-efficiency broadband electronic and optoelectronic devices.

properties,^[5–12] including large absorption coefficient ($\approx 10^5$ cm⁻¹), low trap density, large carrier diffusion length (from 2.6 μ m to 3 mm), high carrier mobility (≈ 100 cm² V⁻¹ s⁻¹), and small exciton binding energy (≈ 20 meV), enable a range of promising applications in optoelectronics and electronics, such as solar cells,^[13–16] transistors,^[17–20] lasers,^[21–24] and light emitting diodes (LEDs).^[25–28] Although great progress has been made for perovskite optoelectronics in the last decade, a deep understanding and control their underlying properties remain limited. For example, the absorption wavelength of common-used perovskites is limited to the UV–vis range. Developing an effective and facile strategy to tune its optical and electronic properties remains as a major challenge.

Introducing ions, molecules, or nanoparticles into perovskites provides more possibilities to tune their optical, electrical, and even mechanical properties. For example, He et al. introduced Cs ions into perovskite, resulting in improved photoelectric conversion efficiency and increased stability.^[29] Lin et al. synthesized perovskite/carbon nanotube composite crystal and achieved improved carrier mobilities.^[30] Coupling perovskites with quantum dots (QDs) provides more interesting phenomena. For example, Sargent's group first developed a mixed perovskite film by introducing PbS QDs into crystalline film and a single crystal bulk, which showed promising light-emitting application in IR region.^[31,32]

1. Introduction

Recently, organic–inorganic metal halide perovskite (ABX₃, A: organic cationic group, B: Pb, Sn, etc., and X: halogen) single crystals have become appealing candidate materials in optoelectronic devices and applications.^[1–4] Their excellent intrinsic

C. Zhao, Y. Zou, W. Kong, T. Huang, Z. Yu, J. Yang, W. Yu
GPL Photonics Lab, State Key Laboratory of Applied Optics
Changchun Institute of Optics, Fine Mechanics and Physics
Chinese Academy of Sciences
Changchun 130033, China
E-mail: weiliyu@ciomp.ac.cn

C. Zhao, Y. Zou, W. Kong, T. Huang, Z. Yu, J. Yang, W. Yu
University of Chinese Academy of Sciences
Beijing 100049, China

 The ORCID identification number(s) for the author(s) of this article can be found under <https://doi.org/10.1002/adom.202101535>.

C. Chen, Y. Han
Advanced Membranes & Porous Materials Center
King Abdullah University of Science and Technology
Thuwal 23955-6900, Kingdom of Saudi Arabia
E-mail: yu.han@kaust.edu.sa

R. Wei, C. Guo
The Institute of Optics
University of Rochester
Rochester, NY 14627, USA
E-mail: guo@optics.rochester.edu

F. Li
School of Physics
The University of Sydney
Sydney, NSW 2006, Australia

DOI: 10.1002/adom.202101535

They established a contactless method for measuring the diffusion length and mobility of the perovskite single crystal by adding PbS quantum dots into single crystals of various mass ratios.^[33] With the efforts of peer researchers, perovskite composites have been utilized in broad application fields including photodetection,^[30,34,35] light-emitting device,^[36–38] and photovoltaic device,^[39–43] with moderate progresses being made. Further exploring, understanding their underlying optical and electrical properties, and developing efficient optoelectronic devices remain limited.

Near-infrared (NIR) photodetectors have extensive research value, which possess a wide range of applications in military and civil fields such as communication,^[44,45] passive night vision,^[46] biosensors,^[47,48] NIR imaging, and radiation measurements.^[49,50] Compared to the UV–vis responsive photodetectors, NIR photodetectors possess the advantages of minimized transmission energy loss for optical fiber communication, night visibility for overnight working, and biocompatibility for biometric systems and disease diagnoses, etc.^[44,46,47] In this regard, breaking the absorption limit of perovskite materials and developing efficient perovskite-based NIR photodetectors are highly attractive across material, chemical, and physical research communities. As certain narrow bandgap semiconductors have shown merits in the field of photoelectric detection, developing NIR-photodetector-coupled perovskite and QDs provides a promising strategy to improve perovskite photodetector's performance in the NIR range.

Ag₂S is a classical semiconductor with the energy bandgap of 0.90–1.10 eV,^[51–53] which can be utilized as detecting and bioimaging materials operating in the NIR range. Here, we synthesized Ag₂S-quantum-dot-in-perovskite (Ag₂S-QDiP) through a laser-assisted inverse temperature crystallization (LA-ITC) method. A vis–NIR broadband photodetector is then fabricated by using these Ag₂S-QDiP matrixes as active layers, which take advantage of synergistic effect of combining Ag₂S QDs' NIR response and MAPbBr₃ single crystal's long diffusion length, high visible absorption coefficient, and low defect density. The resulting photodetectors exhibit the dual-band photoresponse property, with the high photoresponsivity (*R*), photodetectivity (*D*^{*}), and external quantum efficiency (EQE) of 1.17 A W⁻¹, 6.24 × 10¹⁴ Jones, and 273.41% at 532 nm, and 57.69 mA W⁻¹, 1.03 × 10¹¹ Jones, and 4.8% at 1064 nm, respectively. The greatly enhanced photoresponsivity in the NIR wavelength range and the balanced electron and hole mobility can be attributed to the balanced charge transfer and the heterojunction formed between the Ag₂S QDs and the perovskite.

2. Results and Discussions

We synthesized the Ag₂S-QDiP through the LA-ITC method. The scheme of the synthesis device is shown in **Figure 1a** and in Figure S1 (Supporting Information). A 1064 nm continuous wave (CW) laser is utilized as the thermal source. The confined growth space is constituted by the front wall of growth cell and the tightly fitted silicon (Si)/SiO₂ substrate. Precursor solution can be filled into the confined space by capillary effect. Figure 1b shows the temperature distribution of the reaction cell obtained by an infrared imaging thermometer. In the equilibrium state,

the temperature of the laser irradiation center is about 130 °C, and the temperature drops from the center to the periphery. At the edge of the reaction cell, the temperature drops to about 40 °C. The MAPbBr₃ matrix can nucleates accommodating the Ag₂S QDs near the irradiation center. Due to the relatively concentrated energy and temperature gradient, the Ag₂S-QDiP matrixes can nucleate more easily near the irradiation center. It takes about 40 min to incubate a 1 mm × 1 mm Ag₂S-QDiP matrix sample. Moreover, compared to the antisolvent-assisted crystallization method, the ITC method can help the Ag₂S QDs distribute more uniformly into the MAPbBr₃.^[42] By tuning the ratio between the Ag₂S QDs solution and the perovskite precursor solution, Ag₂S-QDiP matrixes with different colors can be obtained. The color of Ag₂S-QDiP transitions changes from orange of pure MAPbBr₃ single crystal to brown as the Ag₂S:MAPbBr₃ incorporation ratio increases (Figure 1c; Figure S2, Supporting Information). As decreasing the thickness of the Ag₂S-QDiP can effectively reduce the trap densities during the fabrication of devices,^[54,55] micrometer-sized Ag₂S-QDiP matrixes on the Si/SiO₂ substrate are obtained through the space confinement method. Optical image (Figure 1d; Figure S3, Supporting Information) shows that the as-prepared Ag₂S-QDiP matrixes are smooth on top with the average thicknesses of 25 μm (Figure 1e; Figure S3, Supporting Information). The scanning electron microscopy (SEM) image (Figure 1f) further confirms the smooth surface morphology of the synthesized Ag₂S-QDiP matrix. Energy dispersive X-ray spectrometry (EDS) measurements are carried out to measure the element distribution of selected area, of which the obtained mapping (Figure S4, Supporting Information) shows that four elements, including silver (Ag), sulfur (S), lead (Pb), and bromine (Br), are distributed evenly in the Ag₂S-QDiP, indicating the uniform dispersion of QDs in the as-prepared samples.

In order to study the influence of adding Ag₂S QDs in the lattice structure of perovskite matrixes, we conducted the X-ray diffraction (XRD) tests for the pure MAPbBr₃ and the Ag₂S-QDiP samples with different mass incorporation ratios (Ag₂S:MAPbBr₃ = 1:1600, 1:1280, and 1:960). The results are shown in Figure 1g, which indicates that the cubic structure of MAPbBr₃ is well preserved after adding Ag₂S QDs to a certain extent, implying that adding Ag₂S QDs with a small ratio does not damage the lattice structure. As shown in Figure S5 (Supporting Information), the as prepared Ag₂S QDs appear as the low temperature phase, namely, α-Ag₂S (monoclinic, JCPDS No. 00-012-0072).^[56,57] In the enlarged XRD pattern (Figure 1h), which shows the fine patterns of (100), (110), and (210) peaks, one can find that the peak positions shifted slightly to the right (i.e., to high diffraction angle) after adding the Ag₂S QDs. The difference of 2θ degrees between MAPbBr₃ and Ag₂S-QDiP is about 0.13 eV for various incorporation ratios. The shift of the XRD patterns indicates that incorporating Ag₂S QDs into the MAPbBr₃ crystal can slightly influence the lattice spacing of the perovskite matrix. The distances of perovskite crystal planes decrease after introducing Ag₂S QDs. When the incorporation ratio further increases to above 1:160, it is difficult to obtain well-crystallized matrixes anymore, indicating that a tolerance limit exists for the content of Ag₂S QDs in the perovskite matrix.

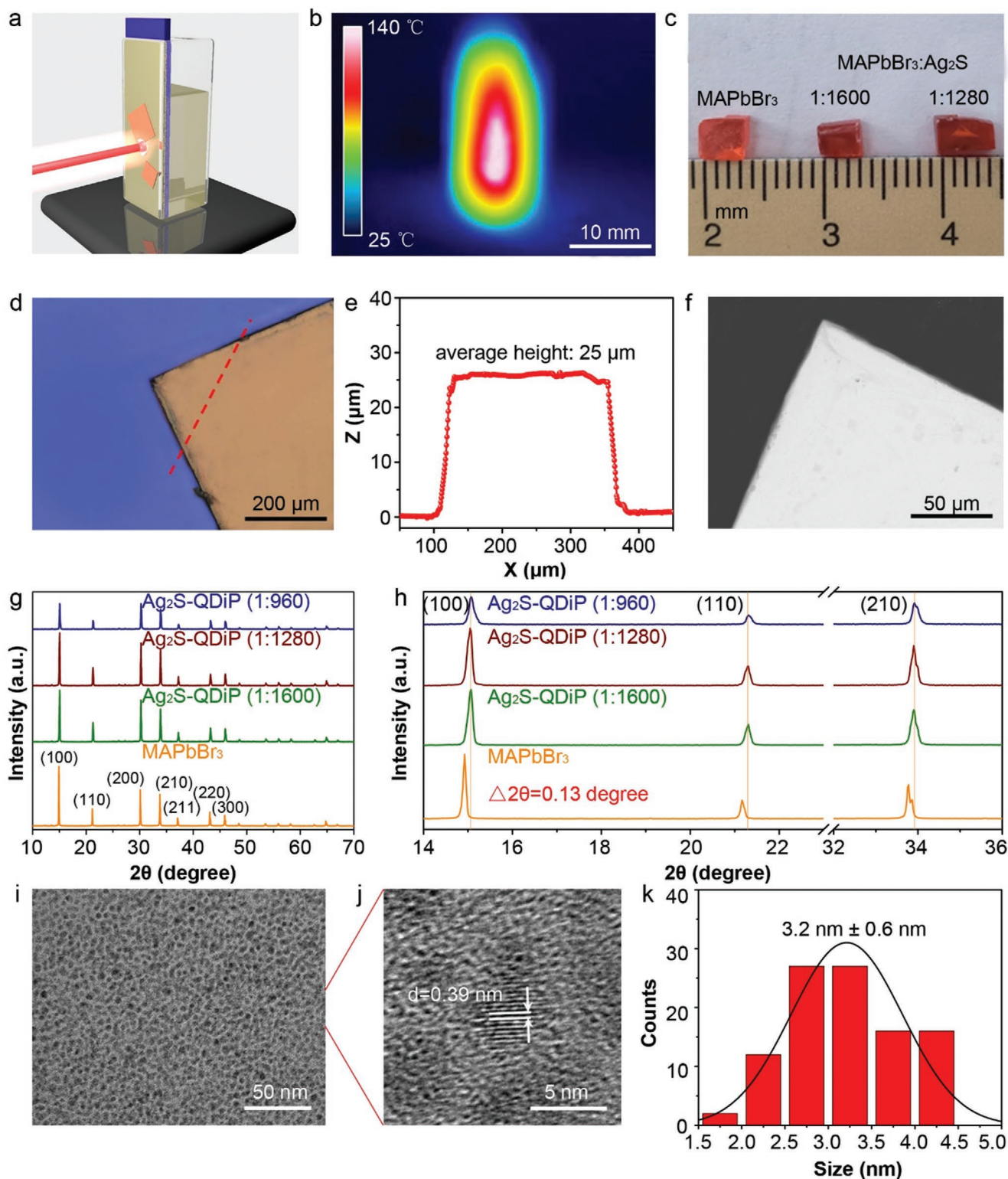


Figure 1. a) Schematic diagram of laser-assisted synthesis of Ag_2S -QDiP matrices. b) Image of the temperature distribution of the reaction cell during the synthesis process (taken by an infrared imaging thermometer). c) The photograph of Ag_2S -QDiP bulk mixed with Ag_2S QDs in different incorporation ratios. d) Optical image of Ag_2S -QDiP matrices with an incorporation ratio of 1:1280. e) Distribution diagram of Ag_2S -QDiP matrix thickness in lateral dimension. f) SEM photograph of Ag_2S -QDiP matrix. g) XRD patterns of Ag_2S -QDiP matrices in different incorporation ratios. h) Detailed XRD patterns of (100), (110), and (210) peaks of Ag_2S -QDiP matrices in different incorporation ratios. i) TEM image of Ag_2S QDs. j) HRTEM image of Ag_2S QDs. k) Statistical histogram of Ag_2S QDs' size distribution.

We then calculated the dot-to-dot spacing (L) in the Ag_2S -QDiP matrixes with different incorporation ratios according to the equation^[33]

$$L = r \times \sqrt[3]{\frac{4}{3} \pi \left(\frac{\rho_{\text{Ag}_2\text{S}}}{\rho_{\text{MAPbBr}_3}} \right) X + 1} \quad (1)$$

where r is the average diameter of the added Ag_2S QDs, estimated to be 3.2 nm according to the transmission electron microscopy (TEM) image and the size distribution statistical histogram (Figure 1i–k). $\rho_{\text{Ag}_2\text{S}}$ is the density of Ag_2S QDs, and the value is 7.2 g cm^{-3} .^[58] ρ_{MAPbBr_3} is the density of perovskite single crystal with a value of 3.5 g cm^{-3} .^[33] X is incorporation ratio. The incorporation ratio used in this paper and the corresponding Ag_2S QDs dot-to-dot spacing is shown in Figure S6 (Supporting Information), which indicates that the dot-to-dot spacing decreases with the increase of Ag_2S QD incorporation ratio.

We then perform the morphological as well as optical characterization of the synthesized Ag_2S -QDiP matrixes and focus on the influence of the amount of Ag_2S QD on its optical properties. As shown in Figure 2a, the TEM image shows the scattered dots with darker contrast distributed in the Ag_2S -QDiP (1:1280), which can be attributed to the added Ag_2S QDs according to

their sizes ($\approx 3 \text{ nm}$). Considering that the ultralow-dose conditions ($10 \text{ e}^- \text{ A}^{-2}$) that we employed for the TEM imaging have been proved to be safe enough for preserving the structure of MAPbBr_3 , the observed scattered dots are unlikely lead bromide (PbBr_2) generated from the electron-beam-induced degradation of MAPbBr_3 matrixes. The high-resolution transmission electron microscopy (HRTEM) image (Figure 2b) and the corresponding fast Fourier transform (FFT) pattern (Figure 2c) confirm that the imaged matrix has an intact perovskite structure without degradation or phase transformation. The EDS elemental mapping result further confirms that Ag_2S QDs are embedded in the MAPbBr_3 (Figure S4, Supporting Information).

By controlling the incorporation ratio between MAPbBr_3 and Ag_2S QDs, the QDs' concentration and the dot-to-dot distance can be easily tuned. The evenly distribution of Ag_2S QDs in perovskite lattice indicates that the crystallization process is thermodynamic stable, and the two materials have fine compatibility. The hardly distinguished interface between Ag_2S QDs and perovskite lattice provides the pathways of efficient charge transfer between these two components, where the photon-generated excitons can be separated.

We evaluate the optical properties of the MAPbBr_3 single crystal and the Ag_2S -QDiPs by measuring their absorption

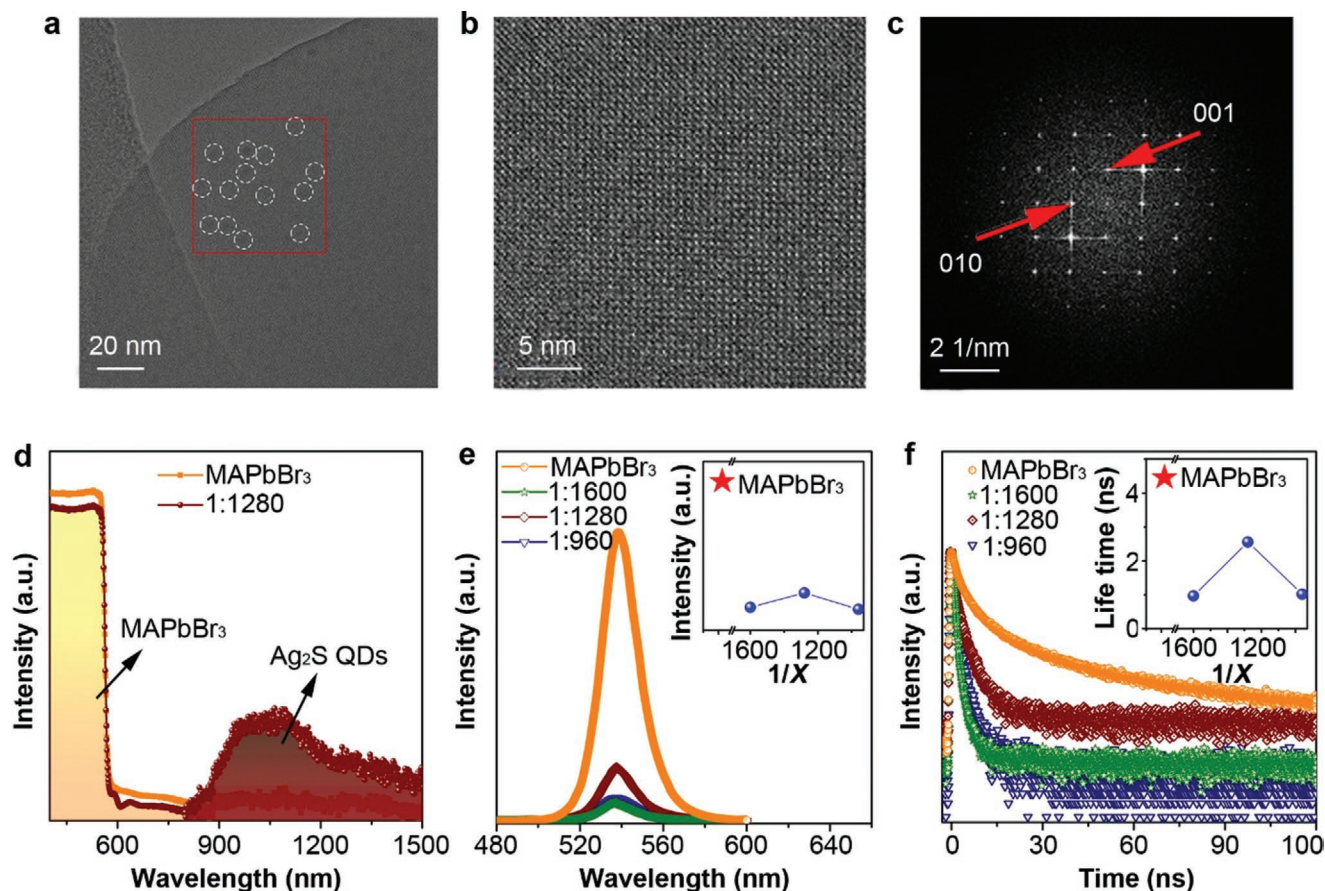


Figure 2. a,b) TEM and HRTEM of Ag_2S -QDiP (1:1280). Ag_2S QDs are circled out by dotted lines in panel (a). c) Indexed FFT pattern of panel (b). d) Vis–NIR absorption spectra of MAPbBr_3 and Ag_2S -QDiP (1:1280). e) PL spectrum (excitation: 473 nm) and f) TRPL spectrum (excitation: 532 nm) of MAPbBr_3 and Ag_2S -QDiP of different incorporation ratios (X). The insets are statistical polylines of peak PL intensity and average lifetime, respectively.

spectra, steady-state photoluminescence (PL) spectra, and time-resolved photoluminescence (TRPL) spectra. The absorption spectrum shows the absorption cutoff wavelength broadens from 550 nm for pure perovskite matrix, which increases to over 1200 nm for Ag₂S-QDiPs with an incorporation ratio of 1:1280, as shown in Figure 2d. This result matches well with the uniform color shown in Figure 1c, indicating that the Ag₂S QDs are evenly embedded in the perovskite matrixes. The steady-state PL properties are shown in Figure 2e and in Figure S7 (Supporting Information). For each sample with specific incorporation ratio, ten points are selected to reduce the experimental errors. The PL spectra of pure perovskites and samples with different incorporation ratios (from 1:1600 to 1:960) are listed in Figure S7 (Supporting Information). As shown in Figure 2e, both the pure perovskite and Ag₂S-QDiP exhibited a PL peak at 538 nm arising from bandgap of the perovskite; however, the PL intensity of the Ag₂S-QDiP is much lower than that of the pristine perovskite. Such a dramatic PL quenching indicates the effective charge transfer from MAPbBr₃ to Ag₂S QDs under illumination. More specifically, the PL quenching phenomenon also shows clear dependence on the incorporation ratio. With the increasing mass proportion of Ag₂S QDs, the PL quenching effect of the perovskite-based mixture matrixes increased accordingly. This may be related to the decrease of the dot-to-dot spacing of Ag₂S QDs in the Ag₂S-QDiP, i.e., the shorter spacing can lead to the more efficient photoinduced charge transfer at the interfaces.

To further study the effect of Ag₂S QDs in perovskite matrixes on their carrier transport properties, we measured TRPL spectra of the pure MAPbBr₃ and the Ag₂S-QDiP with different incorporation ratios to investigate their carrier lifetimes (Figure 2f). For each sample, ten points are randomly selected for the TRPL spectra test, and the data are shown in Figure S8 (Supporting Information). After incorporation of Ag₂S QDs, the average PL lifetime is significantly shortened from 4.52 ns for pure MAPbBr₃ to 2 ns for Ag₂S-QDiP (1:960). With the increase of the mass proportion of Ag₂S QDs, the lifetime of the Ag₂S-QDiP is shortened accordingly. The quenching of steady-state PL and the shortening of the PL lifetime both indicate that in the Ag₂S-QDiP, the photogenerated carriers can be separated at the interface and then transferred between MAPbBr₃ and the Ag₂S QDs efficiently. The PL quenching effect and the resulting PL lifetime attenuation intensify the fastened photoinduced carrier separation process with the increase of Ag₂S QDs' incorporation ratio, that is, the higher ratio of incorporated Ag₂S QDs can result in the lower PL intensity and the smaller average PL lifetime. These findings on carrier transport kinetics further evidence the effective transfer between MAPbBr₃ and Ag₂S QDs in the Ag₂S-QDiP, which is beneficial for fabricating the broadband responsive photodetectors.

We then try to investigate the electronic and optoelectronic properties of the pure perovskite and Ag₂S-QDiP samples. When the samples are illuminated under 532 nm light (within the absorption range of MAPbBr₃), MAPbBr₃ matrix will work as the light absorber. While working in the NIR region (under 1064 nm laser source), the active material would be the embedded Ag₂S QDs instead of MAPbBr₃ matrix. Combining the large diffusion coefficient, long diffusion length, and high carrier mobility, the photogenerated carriers generated from

the Ag₂S QDs will transport in the device and be captured by the electrodes, as shown in Figure 3a. A related charge-transport model for the Ag₂S-QDiP working in the 1064 nm region is shown in Figure 3b. The incident 1064 nm NIR light is not enough to excite free electrons in MAPbBr₃ due to its large bandgap, and thus the conversion between optical and electrical signals cannot be achieved. Meanwhile, when Ag₂S QDs working alone as the photoactive material, a large number of trap states between dots and dots will capture the photogenerated carriers and lead to recombination. Thus, the excitons and/or free charges generated by light excitation will be consumed by the high defect state density. In the designed Ag₂S-QDiP matrix, however, the incident light energy can generate the electron-hole pairs successfully, and then the photoinduced electrons can transport in the channel through the perovskite matrix, exhibiting considerable device performance. Effective conversion and detection of light-generated electrical signal can be achieved eventually.

To study the effect of incorporating Ag₂S QDs in MAPbBr₃ crystals, we tested the defect density and carrier mobility of electrons and holes in MAPbBr₃ and Ag₂S-QDiP matrixes through the space charge limited current (SCLC) method, as shown in Figure 3c–f. The SCLC data indicate that the trap density (both electrons and holes) in the pure perovskite crystal can increase by over two times after mixing with Ag₂S QDs. The electron mobility drops by a third, while the hole mobilities doubled, implying that the incorporation of Ag₂S QDs can tune the major carrier concentration and the charge mobilities (the extracted defect density and carrier mobility of samples are summarized in Table 1 for detail). The mobility tuning mechanism may be attributed to the increased possibility of defect scattering. The balanced electron and hole mobility after incorporating Ag₂S QDs in perovskite matrix will be beneficial for developing ambipolar electronic devices.

We then employed the pure MAPbBr₃ single crystal and the Ag₂S-QDiP matrixes (1:1600, 1:1280, and 1:960), which are all synthesized by the LA-ITC method, to construct the visible and the vis–NIR broadband photodetectors with the planar metal–semiconductor–metal structure.

The photoresponse properties of the Ag₂S-QDiP-based photodetectors are measured under the 532 and 1064 nm light illuminations, respectively, as shown in Figure 4. The detailed test methods are showed in the “Experimental Section.” The energy band structures of MAPbBr₃- and Ag₂S-QDiP-based devices are shown in Figure 4a–c. The MAPbBr₃ is the active material accounts for the photoresponse within the visible region for both the pure MAPbBr₃- and Ag₂S-QDiP-based photodetectors. As shown in Figure 4a,b, the incident photon energy can generate hole–electron pairs in the active perovskite matrixes. Due to the low exciton dissociation energy at room temperature, the photoinduced electrons on conduction band (CB) can easily break free from the Coulomb effect and become the free electrons, which can transport in active channel and then be captured by the electrodes, forming the photoelectrical signals. As shown in Figure 4d,e and in Figure S9 (Supporting Information), in the visible region (532 nm), the current–voltage (*I*–*V*) characterization results indicate that the photodetectors based on the Ag₂S-QDiP matrixes, with the incorporation ratios of 1:1600 (Figure S9b, Supporting Information)

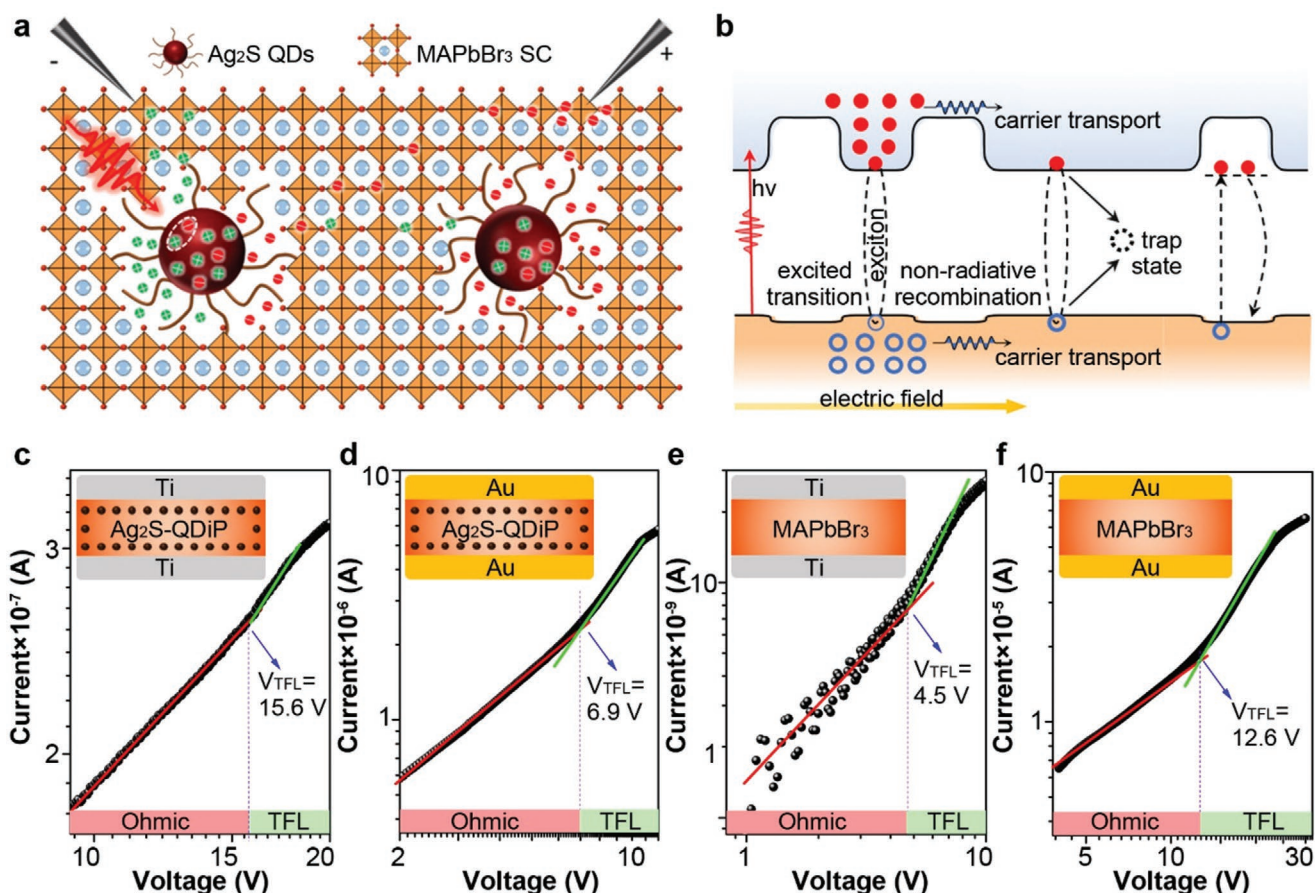


Figure 3. Schematic diagram of a) the charge generation and b) transfer of Ag₂S-QDiP under 1064 nm laser. SCLC curves of Ag₂S-QDiP matrix bulk for c) electrons and d) holes. SCLC curves of MAPbBr₃ single crystal bulk for e) electrons and f) holes.

and 1:1280 (Figure 4e; Figure S9c, Supporting Information), have considerable photoresponse properties comparable with the pure MAPbBr₃-based photodetector. When the incorporation ratio increases to 1:960 (Figure S9d, Supporting Information), the photoresponse performance of the Ag₂S-QDiP-based devices under a 532 nm light irradiation shows the significant decrease under various light intensities. This may be attributed to the high concentration of Ag₂S QDs, which affects the crystal structure and blocks the carrier transport route in MAPbBr₃ to some extent. Figure S10 (Supporting Information) shows the light intensity–photocurrent fitting curves under a bias voltage of ±3 V in a wide range of light intensities extracted from Figure S9 (Supporting Information). In a wide light range, the fitting curve between the photocurrent and the light intensity presents a good linearity, indicating that the recombination loss of the device is relatively low in this range.^[59]

To compare the device performance between the MAPbBr₃- and the Ag₂S-QDiP-based photodetectors in the wide light

band, a 1064 nm CW laser and a white LED are utilized as the light source to test the MAPbBr₃- and Ag₂S-QDiP (1:1280)-based photodetectors, respectively. As shown in Figure 4c, the Ag₂S QDs can work as the photosensitive material in the NIR region (1064 nm), and the MAPbBr₃ matrix can perform as the charge-transporting material. Figure 4f shows the *I*–*V* curves of the Ag₂S-QDiP (1:1280)-based photodetector under different illumination intensities in the NIR range (1064 nm laser). It can be seen from the *I*–*V* curves (Figure S11a, Supporting Information) that when working within the NIR band, the energy of absorbed photon is not enough to excite the electrons in the MAPbBr₃ layer. Thus, the MAPbBr₃-based photodetector does not show any photoresponse performance (Figure S11, Supporting Information). The photodetector based on Ag₂S-QDiP photoactive layer shows greatly improved photoresponse characteristics in the NIR range. Due to the narrow bandgap of Ag₂S QDs, the adsorbed photon energy can excite the electron–hole pairs. The NIR-generated carriers in Ag₂S QDs can

Table 1. Electron (hole) trap density and mobility of MAPbBr₃ and Ag₂S-QDiP (1:1280).

	$n_{\text{trap(electron)}} [\text{cm}^{-3}]$	$n_{\text{trap(hole)}} [\text{cm}^{-3}]$	$\mu_{\text{electron}} [\text{cm}^2 \text{V}^{-1} \text{s}^{-1}]$	$\mu_{\text{hole}} [\text{cm}^2 \text{V}^{-1} \text{s}^{-1}]$
MAPbBr ₃	3.28×10^{11}	1.11×10^{12}	36.42	11.88
Ag ₂ S-QDiP (1:1280)	8.28×10^{11}	2.54×10^{11}	25.86	23.38

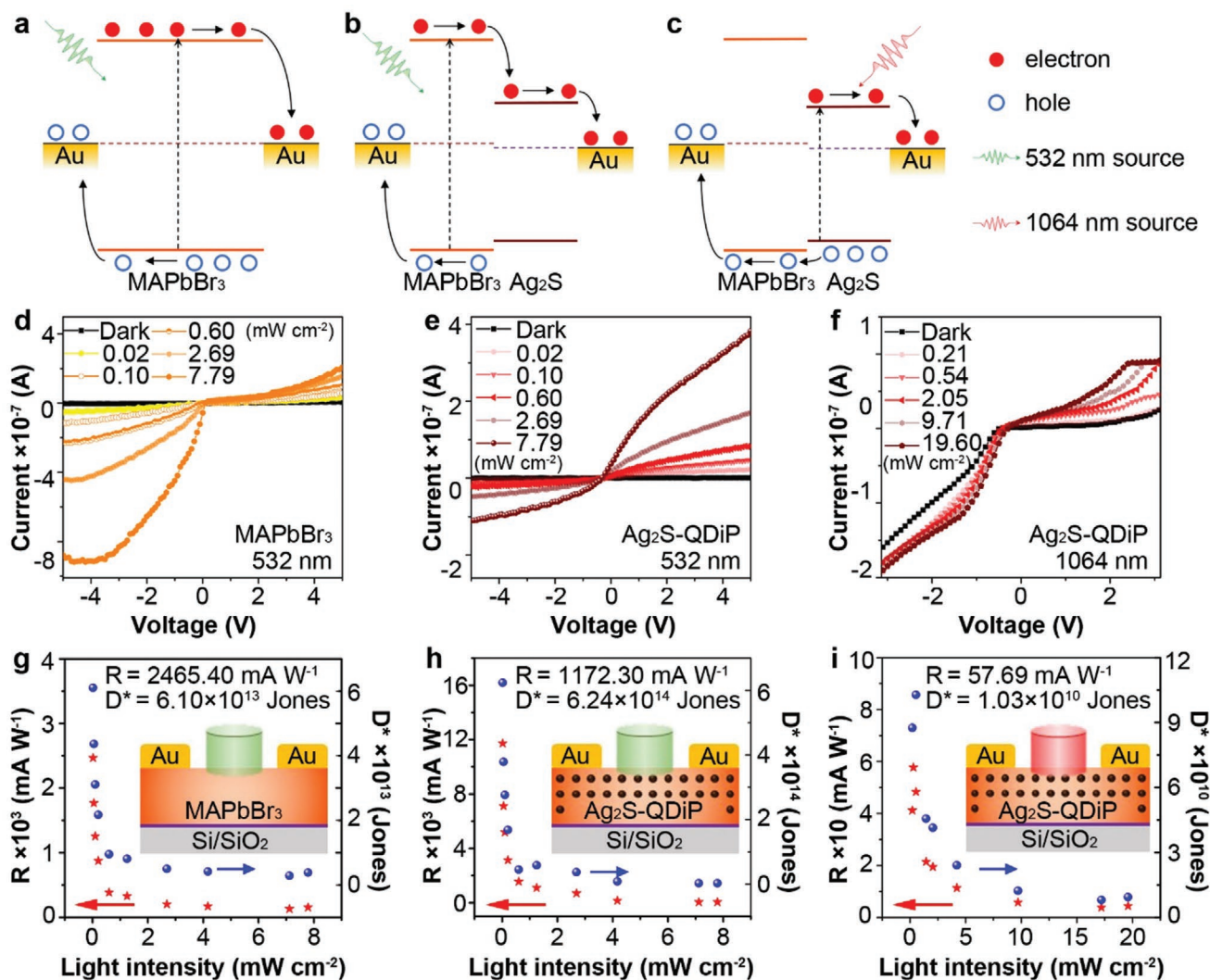


Figure 4. a,b) Bandgap structure of MAPbBr₃- and Ag₂S-QDiP (1:1280)-based photodetector under 532 nm laser. c) Bandgap structure of Ag₂S-QDiP (1:1280)-based photodetector under 1064 nm laser. d,e) *I*-*V* characteristics of MAPbBr₃- and Ag₂S-QDiP (1:1280)-based photodetectors under 532 nm laser with various light intensities. f) *I*-*V* characteristics of the Ag₂S-QDiP (1:1280)-based photodetector under 1064 nm laser with various light intensities. g) Responsivity and detectivity as a function of incident light intensity at bias of -3 V of MAPbBr₃- and Ag₂S-QDiP (1:1280)-based photodetectors under 532 nm laser. h) Responsivity and detectivity as a function of incident light intensity at a bias of +3 V of MAPbBr₃- and Ag₂S-QDiP (1:1280)-based photodetectors under 532 nm laser. i) Responsivity and detectivity as a function of incident light intensity at a bias of +2 V of Ag₂S-QDiP (1:1280)-based photodetector under 1064 nm laser. The illustrations are device structure schemes.

be transferred to the MAPbBr₃ crystal lattice and then transport under the applied bias, and the NIR photons can thus be converted into electrons. Considering the large dot-to-dot distances between Ag₂S QDs within the mixed matrixes (Figure S6, Supporting Information), the discrete heterojunctions between Ag₂S QDs and perovskite can be formed, as shown in Figure 4c. When a positive bias (2 V) is applied, the linear relationship between light intensity and photocurrent is more obvious (Figure S12, Supporting Information).

Interestingly, for the pure MAPbBr₃-based photodetector, the photocurrent value obtained when using a negative bias is greater than the case when applying a positive bias in a wide range of light intensities. In the Ag₂S-QDiP-based photodetector, the situation is just the opposite. The photocurrent obtained when a positive bias is applied is greater than the

photocurrent obtained when a negative bias is applied. The phenomenon indicates that incorporation of Ag₂S QDs in perovskite matrixes can tune the majority carrier concentration, transport, and extraction of carriers in perovskite matrixes under the irradiation conditions.

Then, we calculate three key performance parameters, including photoresponsivity (*R*), photodetectivity (*D**), and EQE, to evaluate the fabricated photodetectors under the 532 and 1064 nm laser irradiations, respectively.

The parameter *R* refers to the photocurrent generated under unit power of the incident light on the effective area, which can be expressed by the following formula^[60]

$$R = \frac{I_{\text{light}} - I_{\text{dark}}}{P \cdot A} \quad (2)$$

where I_{light} is the photocurrent, I_{dark} is the dark current, P is the incident light power density, and A is the effective illuminated area of the device.

The parameter D^* is the photodetectivity of the fabricated devices. When the main source of dark current is dominated by shot noise, the D^* value can be determined by the following equation^[61]

$$D^* = \frac{R}{\sqrt{2qJ_{\text{dark}}}} \quad (3)$$

where q is the charge quantity (value = 1.602×10^{-19} C), and J_{dark} is the dark current density of the as prepared devices.

The EQE is defined as the ratio of the number of detected carriers to the number of photogenerated electron–hole pairs, which can be determined by the formula^[62]

$$EQE = R \frac{hc}{e\lambda} \quad (4)$$

where h is the Planck constant (6.626×10^{-34}), c is the speed of light in vacuum (2.998×10^8 m s⁻¹), q is the charge quantity, and λ is incident light wavelength (532 nm/1064 nm).

According to the above formula, we calculate the R , D^* , and EQE values for the MAPbBr₃- and Ag₂S-QDiP (1:1600, 1:1280, 1:960)-based photodetectors when applying a biased voltage of 3 V, as shown in Figure 4g,h (the data are summarized in Table 2).

The device performance shows a clear dependence on the incorporation ratio of Ag₂S QDs. The Ag₂S-QDiP-based photodetectors with low incorporation ratios (1:1600 and 1:1280) show the similar performance as the pure MAPbBr₃-based photodetectors under a 532 nm laser. When the incorporation ratio is 1:960, we found that the R , D^* , and EQE values of the Ag₂S-QDiP-based photodetector decreases significantly. In order to quantitatively analyze the photodetector performance, we also extracted the R and D^* values from I – V curves of Ag₂S-QDiP-based photodetector in the NIR (1064 nm) range (Figure 4i), and the maximum R , D^* , and EQE values are also listed in Table 2. Briefly, the incorporation of Ag₂S QDs can endow the mixed matrix with obvious enhanced light response characteristics in the NIR range. The enhanced device performance can be attributed to the heterojunctions formed between

MAPbBr₃ and Ag₂S QDs, which improves the light absorption properties and facilitates the efficient charge transfer.

Noticeably, when using white LED as the light source, the MAPbBr₃-based photodetectors show extremely weak photoresponse performance in a wide range of light intensities (Figure S13a,b, Supporting Information). This can be attributed to the small proportion of shorter-wavelength (<550 nm) light from the white LED which can be absorbed by MAPbBr₃; thus, the photocurrent is pretty lower than that of the Ag₂S-QDiP (1:1280)-based photodetector. When the light intensity is below 100 mW cm⁻², the photocurrent cannot be distinguished from the noise. For the Ag₂S-QDiP-based photodetectors, the energy of the light source is concentrated in the absorption band (<1200 nm) of the Ag₂S-QDiP layer, so that the energy can be utilized to generate photogenerated carriers, which will transport in the photoactive layer and then be collected by the electrode under the bias. The I – V curve of the Ag₂S-QDiP-based photodetector shows the considerable photoresponse performance. In addition, in a wide light intensity range, an obvious linear relationship between light intensity and photocurrent can be extracted (Figure S13c,d, Supporting Information). These results indicate that the incorporation of Ag₂S QDs can facilitate the charge transfer via the formed build-in potential in the discrete heterojunction between Ag₂S QDs and MAPbBr₃ and enlarge response region of MAPbBr₃ to the NIR region.

Photoresponse speed is another key parameter of the photodetector, which is extremely important in photoresponse communication systems.^[63,64] The response speeds of the Ag₂S-QDiP (1280)-based photodetector under both visible (532 nm) and NIR (1064 nm) band are evaluated via the time-dependent photoresponse curves. As shown in Figure S14a,c (Supporting Information), the time-dependent photoresponse curves demonstrate that the sensitivity to the incident light of both visible and NIR bands is repeatable and stable. Figure 14b,d (Supporting Information) presents the photoswitch signals of the device. It can be seen that the rise time and decay time of Ag₂S-QDiP-based photodetector are 360 and 200 ms under 532 nm. In the NIR band, the rise time and decay time are 420 and 360 ms under 1064 nm, respectively. The lengthened response time under NIR band can be attributed to the limited charge transfer between the added Ag₂S QDs and MAPbBr₃ substrate. The response speed may be improved by applying a vertical device structure, which will be further optimized in future work.

Table 2. Performance parameters of MAPbBr₃- and Ag₂S-QDiP-based photodetectors with different incorporation ratios under visible light (532 nm) light source.

	R [mA W ⁻¹]	D^* [Jones]	EQE [%]
Visible region (532 nm)			
MAPbBr ₃	2465.40	6.10×10^{13}	575.42
Ag ₂ S-QDiP (1:1600)	1510.22	1.07×10^{14}	348.61
Ag ₂ S-QDiP (1:1280)	1172.30	6.24×10^{14}	273.41
Ag ₂ S-QDiP (1:960)	104.53	2.37×10^{11}	22.68
NIR region (1064 nm)			
MAPbBr ₃	–	–	–
Ag ₂ S-QDiP (1:1280)	57.69	1.03×10^{11}	4.8

3. Conclusion

In conclusion, we synthesized Ag₂S-QDiP matrixes via using the laser-assisted inverse temperature crystallization method, which shows ability to tune the optical and electrical properties of perovskite crystal. The Ag₂S-QDiP-based photodetector exhibited the broadband photoresponse performance, ranging from visible to the NIR region. Compared to the pure MAPbBr₃-based photodetector, the photodetector showed the obviously increased photoresponse properties in the NIR region (around 1064 nm), while maintaining detection performance in the visible range (532 nm). The enhanced R , D^* , and EQE values under a 1064 nm light illumination can be attributed to the balanced electron and hole mobilities, and the discrete heterojunction formed between

Ag₂S QDs and MAPbBr₃ matrix. The balanced electron and hole mobilities in the mixture matrixes are beneficial to carrier transmission and collection, which may trigger more researches on the light emitting, ambipolar electronic devices. Meanwhile, the discrete heterojunction can enhance the light absorption in NIR range and facilitate efficient charge transfer. This research may open up a new door toward developing high-performance broadband optoelectronic devices, and pave the way to tune the optical and electronic properties of perovskite-based electronic and optoelectronic devices.

4. Experimental Section

Chemicals: Methylamine solution (40% aqueous solution, Aladdin), hydrobromic acid (HBr) (40% aqueous solution, Aladdin), PbBr₂ (99%, Aladdin), *N,N*-dimethylformamide (DMF) (99%, Aladdin), silver nitrate (AgNO₃, 99.99%, Sinopharm Chemical Reagent Co., Ltd., Shanghai, China), oleic acid (OA, technical grade, 90%, Sinopharm Chemical Reagent Co., Ltd., Shanghai, China), sublimating sulfur powder (S) (Fuchen (Tianjin) Chemical Reagent Co., Ltd.). Tri-*n*-octylphosphine (TOP, technical grade, 90%), 1-octadecene (ODE, technical grade, 90%, Aladdin), methyl alcohol, butyl alcohol, acetone, toluene (99.5%, Beijing Chemical Industry Group Co., Ltd.), and ethyl alcohol (99.7%, Beijing Chemical Industry Group Co., Ltd.).

Synthesis of Ag₂S Quantum Dots: For synthesizing Ag₂S QDs, 0.68 g of AgNO₃ was dissolved in 4 mL of TOP to obtain Ag-TOP precursor. A mixture of 5.4 g of ODA, 6.4 mL of OA, and 12.8 mL of ODE was combined in a three-necked flask (100 mL), degassed with N₂ to remove water and oxygen, and heated to 70 °C with vigorous stirring until the white powders dissolved. Then 72 mg of S powder was added into the flask with vigorous stirring until the powder was dissolved. About 4 mL of Ag-TOP precursor was quickly injected at 197 °C. The reaction was kept at 167 °C for 4–8 min. Then the growth was quenched by adding 25 mL of butanol, which could also prevent solidification of the reaction mixture. The QDs were isolated by precipitation with ethanol. The isolated QDs were redispersed in toluene. Further purification was implemented to remove excess ligands and impurities. About 30 mL of methanol was added into the product and thoroughly mixed. The mixture was centrifuged, and the precipitate was redispersed in toluene. This step was repeated for three times. Acetone was utilized for further twice purification processes. The purified Ag₂S QDs were dispersed in toluene with a concentration of 50 mg mL⁻¹.

Fabrication of Pure and Ag₂S-QDiP Matrix with the LA-ITC Method: The MABr was synthesized by the previous method by the reaction of HBr and methylamine solution. Then the product was purified and recrystallized by absolute ethanol and diethyl ether. Then 1 M MAPbBr₃ precursor solution was obtained by adding 3.67 g of PbBr₂ and 1.12 g of MABr into 10 mL of DMF. The substrates and growth cells were cleaned by ultrasonic washing in deionized water, ethanol, acetone, and isopropanol for 5 min, respectively. The substrates and growth cells were hydrophilic treated by UV-O₃. The growth cells were treated with trichlorooctadecyl silane for 130 min under 120 °C in a vacuum heating box followed by a cleaning process through ultrasonic washing in acetone and isopropanol and drying with nitrogen. The substrate was inserted into growth cell closely to the front inner wall. Then 3 mL of MAPbBr₃ solution was added into growth cell with various amounts of Ag₂S solution. The 1064 nm CW laser was utilized as the energy source to provide the temperature for inverse temperature crystallization. The laser power was set as 3 W. The MAPbBr₃ and Ag₂S-QDiP matrixes crystallized on the Si/SiO₂ substrate after about 40–60 min.

Characterization: The TEM images were obtained by an H-800 electron microscope with a 200 kV acceleration voltage. The HRTEM image was obtained by a JEM-2100F electron microscope at a voltage of 200 kV. The thickness of micromatrix was measured by a Keyence laser confocal microscope, VK-X1000. The SEM image was performed with Hitachi

S-4800. The X-ray diffraction spectra were utilized to characterize the crystal structure of MAPbBr₃ and Ag₂S-QDiP based on Bruker D8 Focus. The UV–vis–NIR absorption spectra of MAPbBr₃ and Ag₂S-QDiP were carried out by a Cary 5000 spectrophotometer from Agilent Company. PL spectra were obtained from a HORIBA Scientific Raman spectrometer with 2.5 mW cm⁻² laser at 473 nm at room temperature in air. The TRPL spectra were performed on a home-built confocal microscope testing system. The laser source was a pulsed supercontinuum laser (OYSL Photonics, SC-Pro, 150 ps pulse lengths) with a 2 MHz repetition rate. The selected 532 nm beam was focused on the sample after an objective lens (numerical aperture = 0.4) with a power of 0.132 μW. A long-pass filter with an edge of 532 nm was used to cut the pump scattered light from pump laser to detector. The detector was an SPCM-AQRH single photon-counting module (SPCM-AQRH-15, Excelitas Technologies). The lifetime module was TimeHarp 260 P.

MAPbBr₃- and Ag₂S-QDiP-Based Photodetectors: Micromatrix was grown on a Si wafer covered by the SiO₂ oxide layer (250 nm) substrate through the LA-ITC method. Gold (Au) electrodes of 80 nm thick were directly evaporated by a vacuum thermal evaporation method on MAPbBr₃ and Ag₂S-QDiP matrixes with a channel of 500 μm × 100 μm. *I*–*V* curves were measured in the ambient atmosphere at room temperature with a KEITHLEY 4200A Semiconductor Parametric Analyzer and a C-100 probe station (TPSi Company). The laser sources were 1064 and 532 nm CW lasers with tunable laser power. The diameter of laser spot was 2 mm. The exposure time of the device was controlled by an optical shutter (VS2552TO, UNIBILITZ) with a diameter of 2.5 mm.

Supporting Information

Supporting Information is available from the Wiley Online Library or from the author.

Acknowledgements

This work was supported by the National Key Research and Development Program of China (Program No. 2018YFB1107202), the National Natural Science Foundation of China (Grant Nos. NSFC 61774155, 91752025, and 61705227), and the K. C. Wong Education Foundation (Grant No. GJTD-2018-08).

Conflict of Interest

The authors declare no conflict of interest.

Data Availability Statement

The data that supports the findings of this study are available in the supplementary material of this article.

Keywords

Ag₂S quantum dots, doping strategy, perovskites, vis–NIR photodetectors

Received: July 27, 2021
Revised: September 15, 2021
Published online: October 29, 2021

[1] Y. T. Huang, S. R. Kavanagh, D. O. Scanlon, A. Walsh, R. L. Z. Hoyer, *Nanotechnology* **2021**, *32*, 132004.

- [2] L. Dou, Y. M. Yang, J. B. You, Z. R. Hong, W. H. Chang, G. Li, Y. Yang, *Nat. Commun.* **2014**, *5*, 5404.
- [3] L. Chouhan, S. Ghimire, C. Subrahmanyam, T. Miyasaka, V. Biju, *Chem. Soc. Rev.* **2020**, *49*, 2869.
- [4] Z. Fan, K. Sun, J. Wang, *J. Mater. Chem. A* **2015**, *3*, 18809.
- [5] G. C. Xing, N. Mathews, S. Y. Sun, S. S. Lim, Y. M. Lam, M. Gratzel, S. Mhaisalkar, T. C. Sum, *Science* **2013**, *342*, 344.
- [6] S. D. Stranks, G. E. Eperon, G. Grancini, C. Menelaou, M. J. P. Alcocer, T. Leijtens, L. M. Herz, A. Petrozza, H. J. Snaith, *Science* **2013**, *342*, 341.
- [7] C. Wehrenfennig, G. E. Eperon, M. B. Johnston, H. J. Snaith, L. M. Herz, *Adv. Mater.* **2014**, *26*, 1584.
- [8] S. D. Stranks, H. J. Snaith, *Nat. Nanotechnol.* **2015**, *10*, 391.
- [9] H. Wang, D. H. Kim, *Chem. Soc. Rev.* **2017**, *46*, 5204.
- [10] Y. C. Liu, J. K. Sun, Z. Yang, D. Yang, X. D. Ren, H. Xu, Z. P. Yang, S. Z. Liu, *Adv. Opt. Mater.* **2016**, *4*, 1829.
- [11] G. Maculan, A. D. Sheikh, A. L. Abdelhady, M. I. Saidaminov, M. A. Hague, B. Murali, E. Alarousu, O. F. Mohammed, T. Wu, O. M. Bakr, *J. Phys. Chem. Lett.* **2015**, *6*, 3781.
- [12] C. X. Bao, Z. L. Chen, Y. J. Fang, H. T. Wei, Y. H. Deng, X. Xiao, L. L. Li, J. S. Huang, *Adv. Mater.* **2017**, *29*, 1703209.
- [13] W. Peng, L. F. Wang, B. Murali, K. T. Ho, A. Bera, N. Cho, C. F. Kang, V. M. Burlakov, J. Pan, L. Sinatra, C. Ma, W. Xu, D. Shi, E. Alarousu, A. Goriely, H. He, O. F. Mohammed, T. Wu, O. M. Bakr, *Adv. Mater.* **2016**, *28*, 3383.
- [14] M. Saliba, T. Matsui, J. Y. Seo, K. Domanski, J. P. Correa-Baena, M. K. Nazeeruddin, S. M. Zakeeruddin, W. Tress, A. Abate, A. Hagfeldt, M. Gratzel, *Energy Environ. Sci.* **2016**, *9*, 1989.
- [15] M. D. Xiao, F. Z. Huang, W. C. Huang, Y. Dkhissi, Y. Zhu, J. Etheridge, A. Gray-Weale, U. Bach, Y. B. Cheng, L. Spiccia, *Angew. Chem., Int. Ed.* **2014**, *53*, 9898.
- [16] J. X. Chen, D. L. Jia, E. M. J. Johansson, A. Hagfeldt, X. L. Zhang, *Energy Environ. Sci.* **2021**, *14*, 224.
- [17] F. Li, C. Ma, H. Wang, W. J. Hu, W. L. Yu, A. D. Sheikh, T. Wu, *Nat. Commun.* **2015**, *6*, 8238.
- [18] W. L. Yu, F. Li, L. Y. Yu, M. R. Niazi, Y. T. Zou, D. Corzo, A. Basu, C. Ma, S. Dey, M. L. Tietze, U. Buttner, X. B. Wang, Z. H. Wang, M. N. Hedhili, C. L. Guo, T. Wu, A. Amassian, *Nat. Commun.* **2018**, *9*, 5354.
- [19] Y. T. Zou, F. Li, C. Zhao, J. Xing, Z. Yu, W. L. Yu, C. L. Guo, *Adv. Opt. Mater.* **2019**, *7*, 1900676.
- [20] A. M. Zeidell, C. Tyznik, L. Jennings, C. Zhang, H. Lee, M. Guthold, Z. V. Vardeny, O. D. Jurchescu, *Adv. Electron. Mater.* **2018**, *4*, 1800316.
- [21] T. Kondo, T. Azuma, T. Yuasa, R. Ito, *Solid State Commun.* **1998**, *105*, 253.
- [22] B. R. Sutherland, S. Hoogland, M. M. Adachi, C. T. O. Wong, E. H. Sargent, *ACS Nano* **2014**, *8*, 10947.
- [23] J. Guo, T. H. Liu, M. J. Li, C. Liang, K. Y. Wang, G. Hong, Y. X. Tang, G. K. Long, S. F. Yu, T. W. Lee, W. Huang, G. C. Xing, *Nat. Commun.* **2020**, *11*, 3361.
- [24] D. I. Markina, A. P. Pushkarev, I. I. Shishkin, F. E. Komissarenko, A. S. Berestennikov, A. S. Pavluchenko, I. P. Smirnova, L. K. Markov, M. Vengris, A. A. Zakhidov, S. V. Makarov, *Nanophotonics* **2020**, *9*, 3977.
- [25] Z. K. Tan, R. S. Mghaddam, M. L. Lai, P. Docampo, R. Higgler, F. Deschler, M. Price, A. Sadhanala, L. M. Pazos, D. Credgington, F. Hanusch, T. Bein, H. J. Snaith, R. H. Friend, *Nat. Nanotechnol.* **2014**, *9*, 687.
- [26] Y. C. Ling, Z. Yuan, Y. Tian, X. Wang, J. C. Wang, Y. Xin, K. Hanson, B. W. Ma, H. W. Gao, *Adv. Mater.* **2016**, *28*, 305.
- [27] M. Vasilopoulou, H. P. Kim, B. S. Kim, M. Papadakis, A. E. X. Gavim, A. G. Macedo, W. J. da Silva, F. K. Schneider, M. A. M. Teridi, A. G. Coutsolelos, A. B. Yusoff, *Nat. Photonics* **2020**, *14*, 50.
- [28] M. M. Liu, Q. Wan, H. M. Wang, F. Carulli, X. C. Sun, W. L. Zheng, L. Kong, Q. Zhang, C. Y. Zhang, Q. G. Zhang, S. Brovelli, L. Li, *Nat. Photonics* **2021**, *15*, 379.
- [29] W. Chen, Y. C. Zhou, L. Wang, Y. H. Wu, B. Tu, B. B. Yu, F. Z. Liu, H. W. Tam, G. Wang, A. J. Djurišić, L. Huang, Z. B. He, *Adv. Mater.* **2018**, *30*, 1800515.
- [30] C. H. Lin, Z. Lyu, Y. Zhuo, C. Zhao, J. Yang, C. Liu, J. Kim, T. He, L. Hu, F. Li, Y. Shen, K. Liu, W. Yu, T. Wu, *Adv. Opt. Mater.* **2020**, *8*, 2001740.
- [31] Z. Ning, X. Gong, R. Comin, G. Walters, F. Fan, O. Voznyy, E. Yassitepe, A. Buin, S. Hoogland, E. H. Sargent, *Nature* **2015**, *523*, 324.
- [32] H. J. Chen, J. M. Pina, Y. Hou, E. H. Sargent, *Adv. Energy Mater.* **2021**, *11*, 2100774.
- [33] X. W. Gong, Z. Huang, R. Sabatini, C. S. Tan, G. Bappi, G. Walters, A. Proppe, M. I. Saidaminov, O. Voznyy, S. O. Kelley, E. H. Sargent, *Nat. Commun.* **2019**, *10*, 1591.
- [34] D. Zhao, J. Huang, R. H. Qin, G. J. Yang, J. S. Yu, *Adv. Opt. Mater.* **2018**, *6*, 1800979.
- [35] A. A. Bessonov, M. Allen, Y. L. Liu, S. Malik, J. Bottomley, A. Rushton, I. M. Salazar, M. Voutilainen, S. Kallioinen, A. Colli, C. Bower, P. Andrew, T. Ryhänen, *ACS Nano* **2017**, *11*, 5547.
- [36] Z. Y. Yang, O. Voznyy, G. Walters, J. Z. Fan, M. Liu, S. Kinge, S. Hoogland, E. H. Sargent, *ACS Photonics* **2017**, *4*, 830.
- [37] M. Vasilopoulou, H. P. Kim, B. S. Kim, M. Papadakis, A. E. Ximim Gavim, A. G. Macedo, W. Jose da Silva, F. K. Schneider, M. A. Mat Teridi, A. G. Coutsolelos, A. R. bin Mohd Yusoff, *Nat. Photonics* **2019**, *14*, 50.
- [38] X. J. Zhang, X. X. Wu, X. Y. Liu, G. Y. Chen, Y. K. Wang, L. C. Bao, X. X. Xu, X. F. Liu, Q. Zhang, K. H. Yu, W. Wei, J. J. Liu, J. Xu, H. Jiang, P. Wang, X. Wang, *J. Am. Chem. Soc.* **2020**, *142*, 4464.
- [39] V. Q. Dang, M. Byun, J. J. Kang, C. Kim, P. H. Jung, Y. D. Kim, N. E. Lee, H. Lee, *Org. Electron.* **2017**, *50*, 247.
- [40] J. H. Han, S. P. Luo, X. W. Yin, Y. Zhou, H. Nan, J. B. Li, X. Li, D. Oron, H. P. Shen, H. Lin, *Small* **2018**, *14*, 1801016.
- [41] U. Dasgupta, B. Kundu, A. J. Pal, *Sol. RRL* **2018**, *2*, 1800012.
- [42] H. Hosokawa, R. Tamaki, T. Sawada, A. Okonogi, H. Sato, Y. Ogomi, S. Hayase, Y. Okada, T. Yano, *Nat. Commun.* **2019**, *10*, 43.
- [43] H. E. S. Godoy, E. A. Erazo, A. F. G. Reyes, A. H. Khan, S. Agouram, E. M. Barea, R. A. Rodriguez, I. Zarazúa, P. Ortiz, M. T. Cortés, V. M. Sanjosé, I. Moreels, S. Masi, I. M. Seró, *Adv. Energy Mater.* **2020**, *10*, 2002422.
- [44] W. Hu, H. Cong, W. Huang, Y. Huang, L. J. Chen, A. L. Pan, C. L. Xue, *Light: Sci. Appl.* **2019**, *8*, 106.
- [45] Z. X. Liu, L. T. Tao, Y. Z. Zhang, G. Q. Zhou, H. M. Zhu, Y. J. Fang, G. Wu, D. R. Yang, H. Z. Chen, *Adv. Opt. Mater.* **2021**, *9*, 2100288.
- [46] H. Tanaka, T. Yasuda, K. Fujita, T. Tsutsui, *Adv. Mater.* **2006**, *18*, 2230.
- [47] S. Park, K. Fukuda, M. Wang, C. Lee, T. Yokota, H. Jin, H. Jinno, H. Kimura, P. Zalar, N. Matsuhisa, S. Umezue, G. C. Bazan, T. Someya, *Adv. Mater.* **2018**, *30*, 1802359.
- [48] H. E. Nejad, A. Mir, A. Armani, *IEEE Sens. J.* **2019**, *19*, 4874.
- [49] E. H. Sargent, *Adv. Mater.* **2008**, *20*, 3958.
- [50] J. Peng, X. Yue, H. T. Du, Z. H. Yin, M. Y. Chai, D. X. Sun, Y. N. Liu, *Appl. Opt.* **2019**, *58*, 8457.
- [51] X. W. Cheng, Q. F. Cheng, X. Y. Deng, P. Wang, H. L. Liu, *Electrochim. Acta* **2015**, *184*, 264.
- [52] R. Bose, G. Manna, S. Jana, N. Pradhan, *Chem. Commun.* **2014**, *50*, 3074.
- [53] Y. X. Guo, H. W. Lei, B. R. Li, Z. Chen, J. Wen, G. Yang, G. J. Fang, *Rsc. Adv.* **2016**, *6*, 77701.
- [54] J. Xing, C. Zhao, Y. T. Zou, W. C. Kong, Z. Yu, Y. W. Shan, Q. F. Dong, D. Zhou, W. L. Yu, C. L. Guo, *Light: Sci. Appl.* **2020**, *9*, 111.

- [55] J. Xing, Y. Zou, C. Zhao, Z. Yu, Y. Shan, W. Kong, X. Zheng, X. Li, W. Yu, C. Guo, *Mater. Today Phys.* **2020**, *14*, 100240.
- [56] A. Sahu, L. J. Qi, M. S. Kang, D. Deng, D. J. Norris, *J. Am. Chem. Soc.* **2011**, *133*, 6509.
- [57] V. Krylova, N. Dukstiene, *J. Chem.* **2013**, *9*, 987879.
- [58] D. R. Lide, *CRC Handbook of Chemistry and Physics*, CRC Press, Boca Raton, FL **2009**.
- [59] Z. X. Zhang, L. H. Zeng, X. W. Tong, Y. Gao, C. Xie, Y. H. Tsang, L. B. Luo, Y. C. Wu, *J. Phys. Chem. Lett.* **2018**, *9*, 1185.
- [60] C. Xie, C. Mak, X. M. Tao, F. Yan, *Adv. Funct. Mater.* **2017**, *27*, 1603886.
- [61] D. J. Yu, F. Cao, Y. L. Shen, X. H. Liu, Y. Zhu, H. B. Zeng, *J. Phys. Chem. Lett.* **2017**, *8*, 2565.
- [62] J. N. Chen, S. S. Zhou, S. Y. Jin, H. Q. Li, T. Y. Zhai, *J. Mater. Chem. C* **2016**, *4*, 11.
- [63] S. You, L. Zhang, Q. Yang, *Nano Res.* **2021**, *14*, 3386.
- [64] Y. T. Zou, T. T. Zou, C. Zhao, B. Wang, J. Xing, Z. Yu, J. L. Cheng, W. Xin, J. J. Yang, W. L. Yu, H. L. Dong, C. L. Guo, *Small* **2020**, *16*, 2000733.